# CHAPTER 2

# Theoretical Background and Computational Methods

To study a chemical reaction, one needs to get information about energetics and bonding in molecules or between molecules and a catalytic surface. Through electronic structure calculation, one can obtain this information and study the system of interest. With the improvement of the theoretical methods, the electronic structure problem is approximately solved to get the energetics of model catalytic systems at a desirable accuracy level with acceptable computational cost. This chapter briefly introduces theory and models used for electronic structure calculation together with geometry optimization to develop a basic understanding of the catalytic systems studied in this thesis work.

## 2.1 Density functional theory

The accurate description of the structure and dynamics of many-body systems and the solution of the Schrödinger equation is a complex problem in the field of theoretical physics and computational material science. Materials are formed by atoms that in turn are made of nuclei and electrons. The description of the nucleus belongs to classical theory because of the heavy mass as compared to electrons. The strongly localized wave function of the nucleus differs from the electrons which exhibit overlapped orbitals. The interaction of electrons is subjected to both, stationary nuclei in terms of the attractive Coulomb force and the repulsive Coulomb force with neighboring electrons. The interaction phenomenon of electrons specifically makes the electronic structure calculation more complex in terms of many-body problems. To determine the systematic theory for the electronic structure calculations, Hohenberg, Kohn, and Sham established a theory termed density functional theory (DFT). DFT has been recognized as an "enabling technology" for materials modeling [1]. In the formulation of DFT, the electron density distribution function $n(r)$ is used instead of many electrons wave functions $\psi(r_1, r_2, r_3 \ldots\ldots\ldots r_N)$ to determine the ground state energy E for any system consisting of N nuclei and electrons [2].

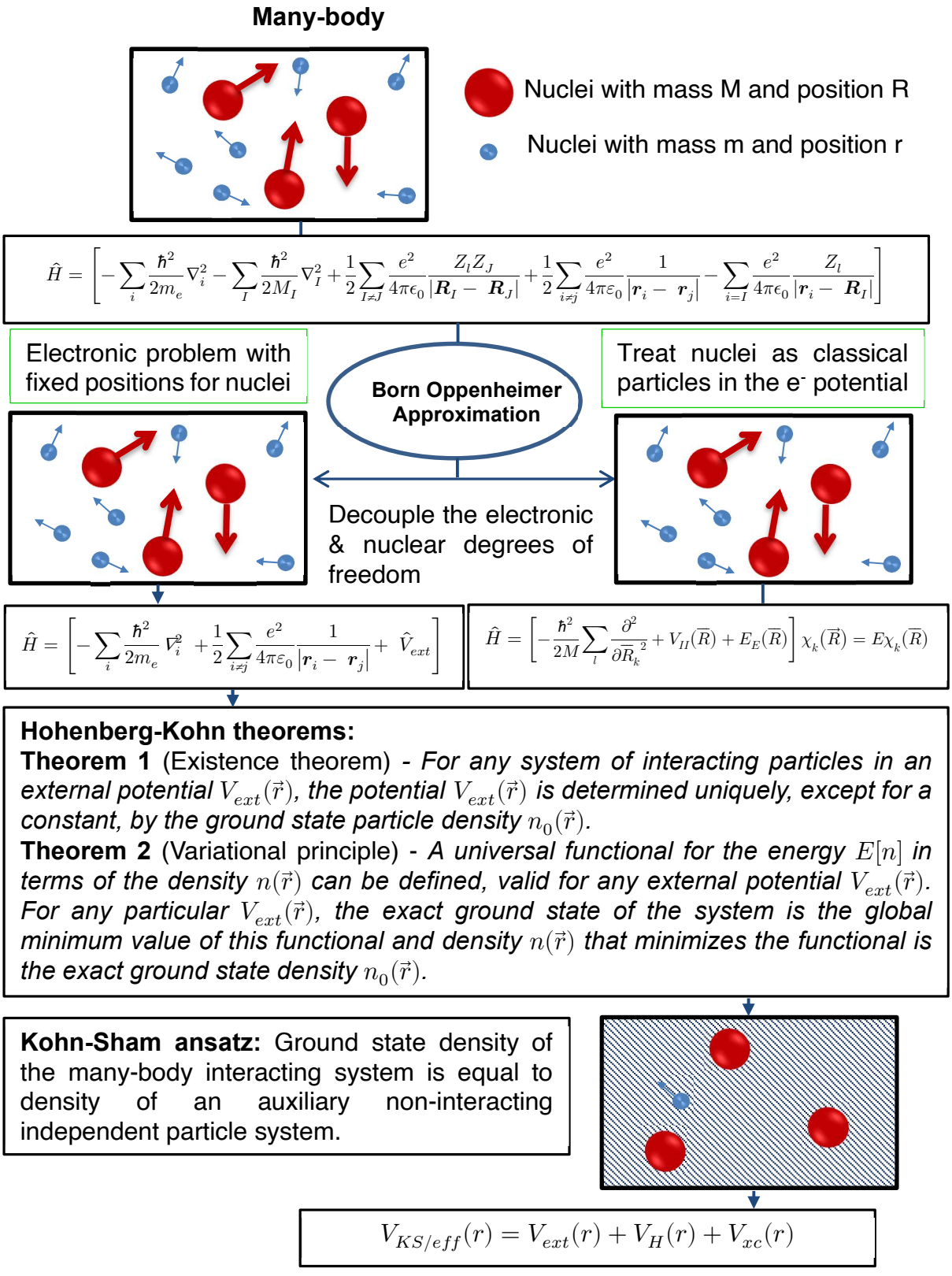


Figure 2.1: From many-body problem to density functional theory (DFT). Born-Oppenheimer approximation, Hohenberg-Kohn theorem and Kohn-Sham ansatz.

This reduces the solution of a many-body problem to that of a single-particle Schrödinger equation with ground-state density distribution. Any crystalline material can be treated as a system of heavy nucleus and electrons interacting with each other based on quantum mechanics. The ground state energy of this system can be evaluated by solving the corresponding many-body Schrödinger equation [3]:

$$\hat{H}\psi = E\psi \tag{2.1}$$

where $\hat{H}$ is the many particles Hamiltonian, $\psi$ is the many-body wave function and E is the ground-state total energy. In the case of a hydrogen (H) atom which possesses one electron and one proton, one can solve the above equation exactly. However, for the crystal structures with many electrons and ions systems, it is treated with complex interactions of the electron and ions. The Hamiltonian for such a system of interacting electrons and nuclei can be written as follows:

$$\hat{H} = \hat{T}_e + \hat{T}_n + \hat{V}_{nn} + \hat{V}_{ee} + \hat{V}_{en} \tag{2.2}$$

where $\hat{T}_n$ and $\hat{T}_e$ are the kinetic energy operator for the nuclei and electrons, respectively. $\hat{V}_{ee}, \hat{V}_{en}$, and $\hat{V}_{nn}$ are the electrostatic potential energy operators for electron-electron, electron-nuclei, and nuclei-nuclei interactions respectively. The many-body Schrödinger equation can be rewritten as:

$$\hat{H}\psi = \left[ -\sum_i \frac{\hbar^2}{2m_e}\nabla_i^2 - \sum_I \frac{\hbar^2}{2M_I}\nabla_I^2 + \frac{1}{2}\sum_{I\neq J} \frac{e^2}{4\pi\epsilon_0}\frac{Z_l Z_J}{|\boldsymbol{R}_I - \boldsymbol{R}_J|} + \frac{1}{2}\sum_{i\neq j} \frac{e^2}{4\pi\varepsilon_0}\frac{1}{|\boldsymbol{r}_i - \boldsymbol{r}_j|} - \sum_{i=I} \frac{e^2}{4\pi\epsilon_0}\frac{Z_l}{|\boldsymbol{r}_i - \boldsymbol{R}_I|} \right] \psi = E\psi \tag{2.3}$$

where $i, j$ are the indices consecutively for electron and nuclei, $m_e$, $M_I$ are the mass of electron and nuclei respectively, $Z_I$, $Z_J$ defines the charges on different nuclei, $\boldsymbol{R}_I - \boldsymbol{R}_J$, $\boldsymbol{r}_i - \boldsymbol{r}_j$ and $\boldsymbol{r}_i - \boldsymbol{R}_I$ are the distances between nuclei-nuclei, electron-electron, and electron-nuclei respectively. The solution of Equation 2.1 gives the energy eigenstates i.e., the total energy of the system. Hence, the solution of the above equation is computationally costly and the solution is computationally feasible only for simple

systems. Therefore, some approximation is essential to determine the properties of complex systems. The stepwise improvement from many-body problem to density functional theory is presented in Figure 2.1 which includes Born-Oppenheimer approximation, Hohenberg-Kohn theorem, and Kohn-Sham ansatz [4-8].

## 2.2 The Kohn-Sham theory

The basic interest is to calculate the ground state energy of many-electron systems through solving the many-body Schrödinger equation given in Equation 2.3. For a system with N electrons, there exist 3N variables leading to the complex solution of Equation 2.3. The DFT depends on a density-based method where the interaction energy and potentials depend only on the density of electrons which decreases the computational cost. The approach of Kohn and Sham [7], published in 1965, turns DFT into a practical tool to obtain the ground state. The Kohn-Sham method is based on parameterization of the density $n(\vec{r})$ in terms of one-electron orbitals $\phi_i(\vec{r})$ (the summation is over all occupied states):

$$n(\vec{r}) = \sum_i \phi_i^*(\vec{r})\,\phi_i(\vec{r}) \tag{2.4}$$

and decomposition of the total energy functional according to:

$$E[n] = T[n] + E_H[n] + E_{xc}[n] + E_{ext}[n] \tag{2.5}$$

where,

$$E_H = \iint \frac{n(\vec{r})n(\vec{r}')}{|\vec{r} - \vec{r'}|}\, d(\vec{r})d(\vec{r}') \tag{2.6}$$

is the electrostatic electron-electron interaction in the Hartree approximation. Here,

$$E_{ext} = \int V_{ext}(\vec{r})\, n(\vec{r})d(\vec{r}) \tag{2.7}$$

describes the interaction with the external field.

The contribution of the kinetic energy is approximated by that of non-interacting electrons in states $\phi_i(\vec{r})$,

$$T[n] = \sum_i \int \phi_i^*(\vec{r}) \left(-\frac{1}{2}\vec{\nabla}^2\right) \phi_i(\vec{r})\, d^3r \tag{2.8}$$

All other contributions to the total energy are described by the so-called exchange-correlation energy $E_{xc}[n]$. The one-electron orbitals are the variational quantities. Variation of the total energy functional $E[n]$ with respect to $\phi_i^*(\vec{r})$ leads to an effective one-electron equation for the determination of the $\phi_i(\vec{r})$, the Kohn-Sham equations:

$$\left(-\frac{1}{2}\vec{\nabla}^2 + \int \frac{n(\vec{r}')}{|\vec{r} - \vec{r'}|} d^3r' + V_{ext}\vec{r} + \frac{\delta E_{xc}[n(\vec{r})]}{\delta n(\vec{r})}\right) \phi_i(\vec{r}) = \varepsilon_i \phi_i(\vec{r}) \tag{2.9}$$

The Kohn-Sham equations that describe electrons moving in a one-electron potential is given by

$$V_{eff}(\vec{r}) = V_{ext}(\vec{r}) + \int \frac{n(\vec{r'})}{|\vec{r} - \vec{r'}|} d^3r' + V_{xc}[n(\vec{r})] \tag{2.10}$$

where the exchange-correlation potential is given by the variational derivation of the exchange-correlation energy,

$$V_{xc}[n(\vec{r})] = \frac{\delta E_{xc}[n(\vec{r})]}{\delta n(\vec{r})} \tag{2.11}$$

The Kohn-Sham equation can be simplified to the following form,

$$\left(-\frac{1}{2}\vec{\nabla}^2 + V_{eff}(\vec{r})\right) \phi_i(\vec{r}) = \varepsilon_i \phi_i(\vec{r}) \tag{2.12}$$

The $\varepsilon_i$ in Eqn. (2.9) are introduced as Lagrange parameters to preserve the orthogonality of the one-electron Kohn-Sham orbitals

$$\int \phi_i^*(\vec{r})\,\phi_j(\vec{r})d^3r = \delta_{ij} \tag{2.13}$$

they are not true excitation energies.

The flowchart for solving the Kohn-Sham equation to achieve self-consistency is illustrated in Figure 2.2.

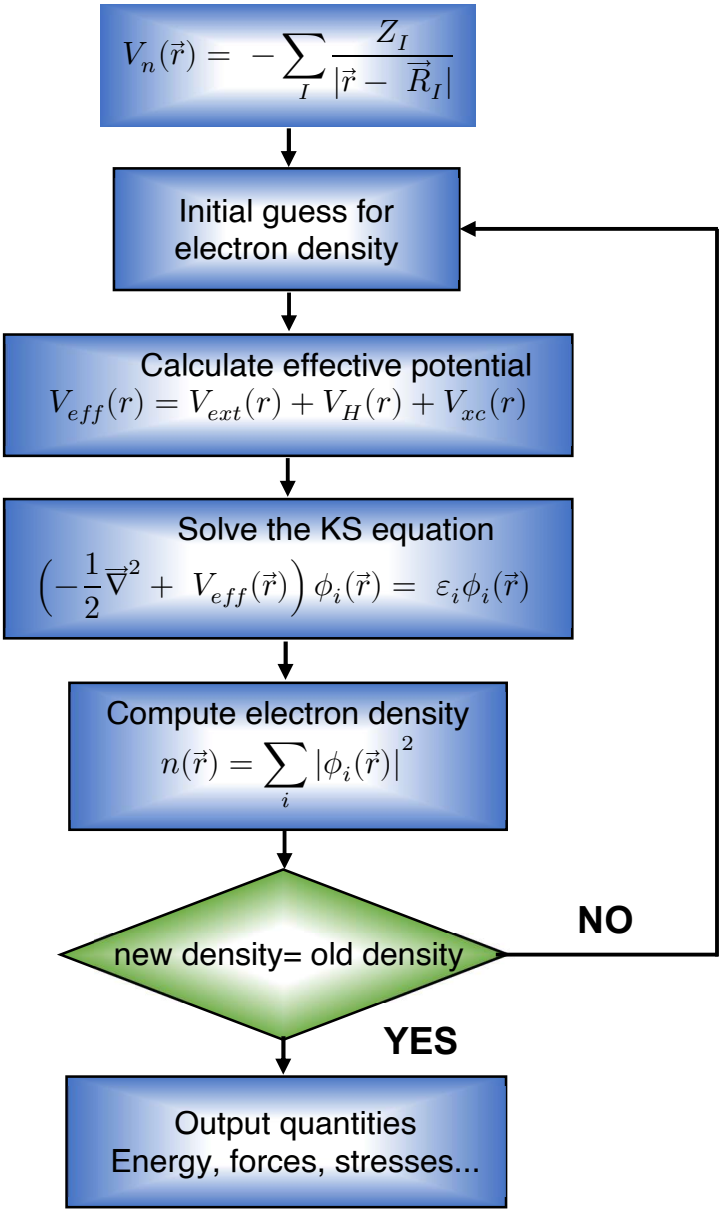


Figure 2.2: Schematic flowchart for finding self-consistent solutions of the Kohn-Sham equations.

### 2.2.1 Exchange and correlation functionals

The accuracy of the Kohn-Sham approach depends largely on the exchange-correlation functional $E_{xc}[n]$. Kohn and Sham noticed that electrons in solids can often be considered to be close homogeneous electron gas, meaning that the effects of exchange and correlation are local. This gives rise to the local density approximation (LDA),

$$E_{xc}^{LDA}[n] = \int \epsilon_{xc}^{hom}\big(n(\vec{r})\big)n(\vec{r})d\vec{r} \tag{2.14}$$

where $\epsilon_{xc}^{hom}$ is the energy of the exchange-correlation (xc) hole in the homogeneous electron gas of density $n$ [8-9].

A chemical system normally involves molecules which means a bigger change in density. Hence, It is not until the development of generalized-gradient approximates (GGAs), DFT is widely used in studying chemical reactions. The GGA type of xc energy depends both on the density and its gradient, which gives a big improvement over LDA.

$$E_{xc}^{GGA}[n] = \int n(\vec{r})\epsilon_{xc}^{hom}\big(n(\vec{r}), \nabla n(\vec{r})\big)d\vec{r} \tag{2.15}$$

Different flavors of GGA functionals have been developed, most notable ones are Perdew-Burke-Ernzerh (PBE) [10], Perdew-Wang 91(PW91) [11], revised Perdew-Burke-Ernzerh (revPBE) [12] and revised Perdew-Burke-Ernzerh (RPBE) [13].

### 2.2.2 Plane-wave and pseudopotentials

The electron orbitals used to express the single-particle density as defined in Kohn-Sham equations may be expanded in terms of any convenient basis set. In practice, a plane wave basis set based on the Bloch theorem is used with several benefits:

$$\psi_{\vec{k}}^{n}(\vec{r}) = \sum_{\vec{K}} c_{\vec{K}}^{n,\vec{k}} e^{i(\vec{k}+\vec{K})\cdot\vec{r}} \tag{2.16}$$

- A plane-wave basis set is unbiased, it does not assume any preconceptions on the form of the problem.
- Due to the Bloch theorem, plane-waves are the natural choice for the representation of electron orbitals in a periodic system.
- The kinetic energy operator is diagonal in a plane-wave representation. Similarly, the potential is diagonal in real space. The use of Fast Fourier Transforms (FFT) in changing between these representations provides a large saving in computational cost.

The main disadvantage of a plane-wave basis set is its inefficiency. The number of basis functions required to describe atomic wavefunctions accurately near a nucleus would be enormous. This difficulty is overcome by the use of pseudopotentials [14], which represent the potential of the ionic cores. This approximation is based on the assumption that only the valence electrons have a significant effect on the physical and chemical properties of the system. The pseudopotential represents the potential of the nucleus and the core electrons subject to the following conditions:

- The valence wavefunction remains unchanged outside the core region (beyond $r_c$ boundary).
- The pseudo wavefunction within the core matches correctly at the boundary.
- The pseudo wavefunction, as well its first derivative, must be continuous at the boundary:

$$\phi^{PS}(r)|_{r=r_c} = \phi^{AE}(r)|_{r=r_c} \wedge \frac{\partial \phi^{PS}}{\partial r}(r)|_{r=r_c} = \frac{\partial \phi^{AE}}{\partial r}(r)|_{r=r_c} \tag{2.17}$$

(The indices PS and AE stand for pseudo and all-electron energies, respectively). The pseudo wavefunction is nodeless within the core region.

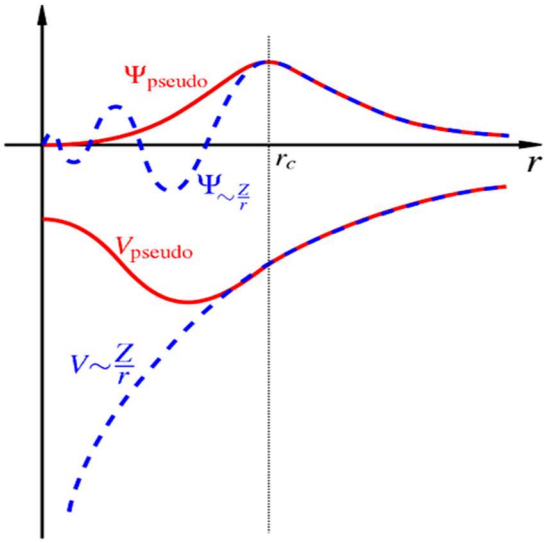


Figure 2.3: Comparison of a wavefunction in the Coulomb potential of the nucleus (blue) to the one in the pseudopotential (red). The real and the pseudo wavefunction and potentials match above a certain cut-off radius (core radius) $r_c$. Sketch inspired by Ref. [17].

The graphical representation of the behavior of a wave function and potential is depicted in Figure 2.3 [15]. All the above-mentioned basic criteria have to be fulfilled for the pseudopotential to be usable. Further criteria have to be introduced for constructing various classes of pseudopotentials, such as ultra-soft (or Vanderbilt) pseudopotentials (USPP), norm-conserving pseudopotentials (NCPP), etc. The so-called projector-augmented wave method (PAW) [16] is an improvement of the pseudopotential technique approach and was originally developed by P. Bloch [17]. It is based on a transformation of the pseudo wavefunction to the all-electron wavefunction. The all-electron wavefunction $\psi$ consists of three parts:

$$\psi = \tilde{\psi} + \sum_{i}^{n} c_i \phi_i - \sum_{i}^{n} c_i \tilde{\phi}_i \tag{2.18}$$

where $\tilde{\psi}$ is the pseudo wavefunction, $\boldsymbol{\phi}_i$ are the all-electron partial waves and $\tilde{\phi}_i$ are the pseudo partial waves. A tilde is used to distinguish between the all-electron (AE) quantities and the pseudo (PS) quantities (such as $\tilde{\psi}$ ) representing only one part of the AE solution. The PS wavefunction is represented by plane-waves that are a good description of the wavefunction in regions far away from the nuclei but deviates

significantly from the AE wavefunction near the nucleus. Hence the AE partial waves $\phi_i$ are introduced to correct this error. These AE partial waves are calculated once as solutions of the radial part of the Schrodinger equation for the isolated atoms. Inside the so-called augmented (core) region, they deviate from the PS wavefunction, however outside this region they match. The AE partial waves ensure that the nodal structure of the wave function is physically correct near the nucleus. The contribution of the PS partial waves $\tilde{\phi}_i$, which are located near the atomic nuclei is subtracted from the PS wavefunction since this region is already included in the AE partial waves. Similar to the AE partial waves, the $\tilde{\phi}_i$ are constructed as solutions of the radial Schrödinger equation for isolated atoms fitted to match the PS wavefunction.

### 2.2.3 Geometry optimization

The calculations in this thesis concern exclusively optimized structures. Geometry optimization was performed by the minimization of the inter-atomic forces. Forces were calculated based on the Hellmann-Feynmann theorem [18] and fed into a Broyden-Fletcher-Goldfarb-Shanno (BFGS) optimizer [19]. A structure was considered optimized when none of the inter-atomic forces exceeded the limit of 0.001 to 0.0001 eV/Å.

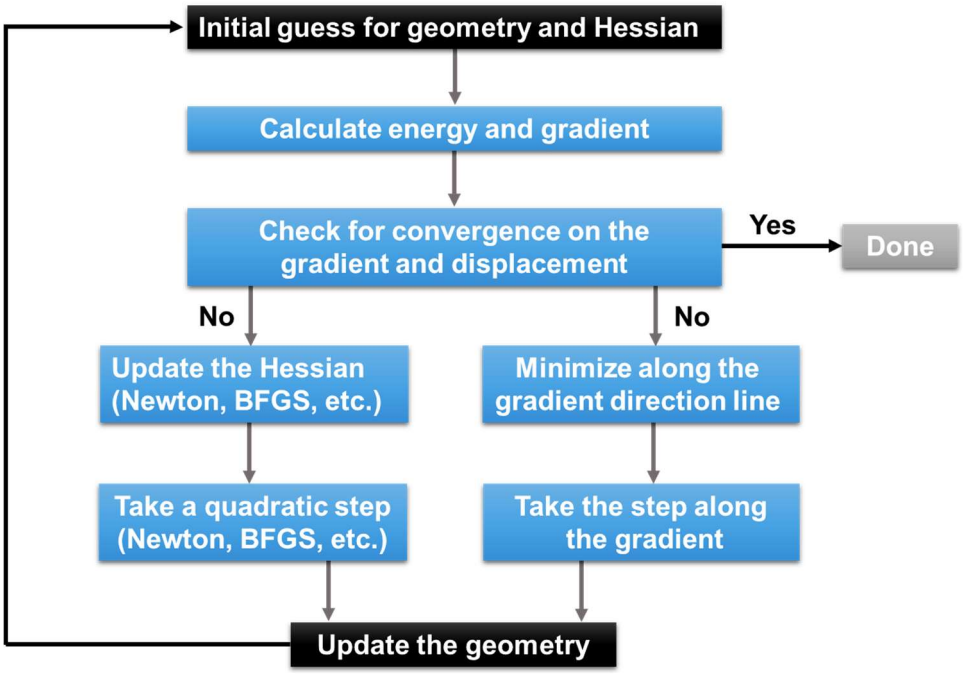


Figure 2.4: Flowchart of Geometry optimization.

The process of geometry optimization in the form of a flowchart is presented in Figure 2.4 [20]. The Hohenberg-Kohn theorems and the Kohn-Sham equations can be extended to include spin, which makes it possible to treat magnetic systems [21-22]. It is possible to treat the spin-polarized system as if it had two different densities one for spin-up and one for spin-down.

### 2.2.4 van der Walls corrections

The standard DFT (with LDA and PBE) framework cannot provide an accurate description of the long-range dispersion forces i.e., very much required for the accurate prediction of the adsorption properties of molecules over transition metal systems. For the treatment of the long-range dispersion forces, the semi-empirical van der Waals corrections D2 and D3 proposed by S. Grimme [23-24] were employed. The sum of the total energy of self-consistent DFT ($E_{KS-DFT}$) with the vdW correction ($E_{disp}$) is given by,

$$E_{DFT+D2/D3} = E_{KS-DFT} + E_{disp} \tag{2.19}$$

**DFT-D2 scheme.** Adds a semiempirical dispersion potential (~$C_6R^{-6}$) to the conventional Kohn–Sham DFT energy ($E_{KS-DFT}$) with a suitable damping function ($f_{damp}$) at small atomic distances. The dispersion correction has the form,

$$E_{disp} = -S_6 \sum_{i=1}^{N_{at}-1} \sum_{j=i+1}^{N_{at}} \frac{C_6^{ij}}{R_{ij}^6} f_{dmp}(R_{ij}) \tag{2.20}$$

**DFT-D3 scheme.** Adds two-body, $E^{(2)}$, and three-body, $E^{(3)}$, energies to the conventional Kohn–Sham DFT energy ($E_{KS-DFT}$). The dispersion correction has the form $E_{disp} = E^{(2)} + E^{(3)}$. The $E^{(2)}$ and $E^{(3)}$ terms are given by the equations

$$E^{(2)} = \sum_{AB} \sum_{n=6,8,1\ .....} s_n \frac{C_n^{AB}}{r_{AB}^n} f_{d,n}(r_{AB}) \tag{2.21}$$

$$E^{(3)} = \sum_{ABC} f_{d,(3)}(\bar{r}_{ABC)}) E^{ABC} \tag{2.22}$$

Here, $S_n$ (also $S_6$ in D2 correction) is a global scaling factor that depends only on the selected exchange-correlation functional (e.g., $S_6 = 1.00$ and $S_8 = 0.72$ for the PBE functional), $C_6^{ij}(and\ C_n^{AB})$ denotes the averaged n$^{th}$ - order dispersion coefficients for each $ij$(and AB) pair, $R_{ij}\,(and\ r_{AB})$ is the interatomic distance between the $i$ and $j$ (A and B) atoms, $f_{dmp}(and\ f_{d,n})$ is a damping function employed to avoid near-singularities for small $r_{AB}$ distances, $\bar{r}_{ABC}$ is the average radii of atom triples $ABC$, and $E^{ABC}$ is the nonadditive triple dipole dispersion term.

## 2.3 Analysis of the electronic properties

There are powerful tools for analyzing the electronic structure and properties offered by state-of-the-art computational materials science. Few of them will be mentioned here, in particular, the density of states and charge density analysis.

### 2.3.1 Density of states (DOS)

An important quantity for many purposes is the density of states (DOS) per unit of energy E (and per unit of volume $\omega$ in the extended matter) [15],

$$g(E) = \frac{1}{N_k}\sum_i\sum_{\vec{k}}\delta(\varepsilon_{i,\vec{k}} - E) = \frac{\omega_{cell}}{(2\pi)^d}\int_{BZ}\delta\left(\varepsilon_{i,\vec{k}} - E\right)d\vec{k} \tag{2.23}$$

In the case of independent-particle states, where $\varepsilon_{i,\vec{k}}$ denotes the energy of an electron (or phonon), $n(E)$ from Eqn. (2.23) is the number of independent-particle states per unit of energy. In principle, the calculation of integral in Eqn. (2.23) is not a trivial task. Three popular types of methodologies for this Brillouin zone integration are mentioned here: namely the linear tetrahedron method (LTM) by Jepsen and Andersen [25], modified tetrahedron method (MTM) by Bloch et al. [26], and the Gaussian broadening method (GBM) by Methfessel and Paxton [27]. Figure 2.5 illustrates the schematic general form of the DOS for bulk, 2D, 1D, and 0D materials.

The total density of states as defined by Eqn. (2.38) is a projection of all bands of the electronic band structure over all k-points. As one wishes to analyze space-resolved DOS in the real space, the local density of states (LDOS) may be defined as follows:

$$g(\vec{r}, E) = \sum_i \sum_{\vec{k}} |\psi_{i\vec{k}}(\vec{r})|^2 \delta(\varepsilon_{i,\vec{k}} - E) \tag{2.24}$$

To study the interaction of atoms with each other, we define the projected density of states (PDOS):

$$g(\alpha, E) = \sum_i \sum_{\vec{k}} |\langle \psi_{\alpha\vec{k}}(\vec{r}) | \psi_{i\vec{k}}(\vec{r}) \rangle|^2 \delta(\varepsilon_{i,\vec{k}} - E) \tag{2.25}$$

where $\psi_{\alpha\vec{k}}$ denotes orthonormal states to $\psi_{i\vec{k}}$. The PDOS is in principle a projection of the DOS onto atomic orbitals. When plotting DOS spectra, attention is given to the position of the zero-point.

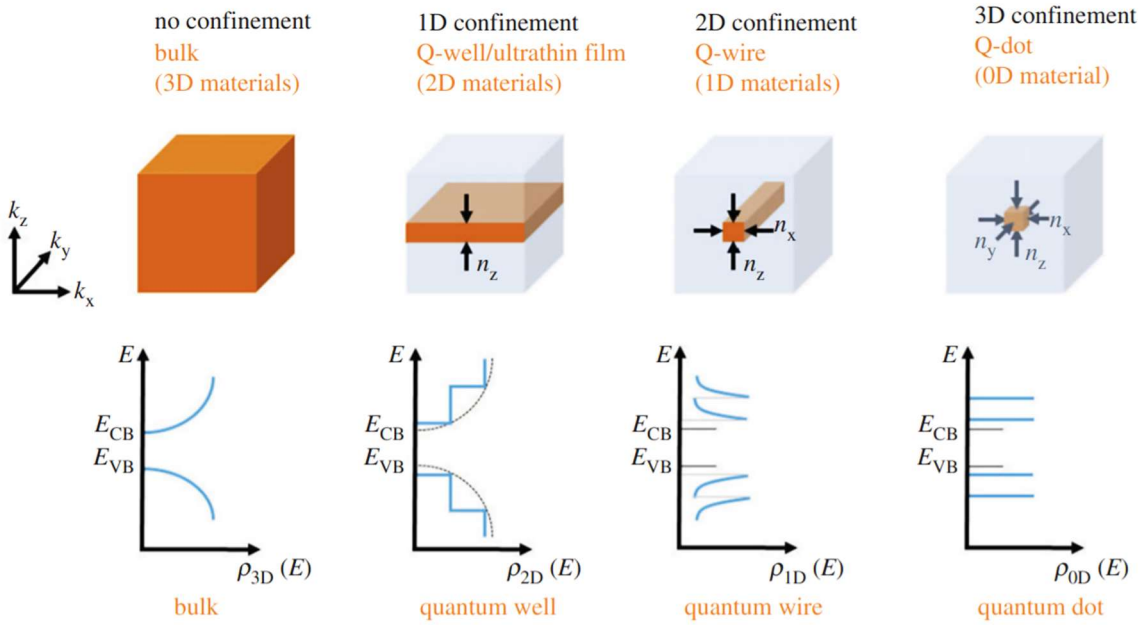


Figure 2.5: Schematic illustration of broken symmetry and functional form of the density of states in 1D, 2D, and 3D confined materials [28].

The Fermi Energy $E_F$ refers to the energy of the highest occupied quantum state in a system of fermions at absolute zero temperature. As the Fermi energy $E_F$ appears in all DOS spectra, it is shifted to zero energy level in periodic systems, where the spectrum is usually continuous. For molecules or other localized clusters, the Fermi

energy is arbitrarily shifted to the value $E_F = \frac{1}{2}(E_{HOMO} + E_{LUMO})$, i.e., the average value between the lowest unoccupied (LUMO) and highest-occupied (HOMO) electronic state. Molecules usually have electronic states at discrete energy values, thus giving a straight line.

### 2.3.2 Charge density analysis

The charge density in general is defined as the amount of charge in a specified volume. As it depends on the position vector $\vec{r}$, in quantum mechanics, it can refer to the spatial charge distribution over the volume of a molecule or a unit cell of a periodic solid. The electronic charge density is related to the wavefunction by the equation,

$$n(\vec{r}) = e^2 \sum_{n\vec{k}\in occ} |\psi_{n\vec{k}}(\vec{r})|^2 \tag{2.26}$$

Where $e$ is the charge of an electron ($e = 1.6021733 \cdot 10^{-19}$ Coulomb), $\psi_{n\vec{k}}(\vec{r})$ is the wavefunction of the $n^{th}$ electron band and the sum in (2.26) goes over occupied electronic states only. The visualization of the charge density helps elucidate the bonding of atoms to each other and it is preferably made by the means of plotting 3D iso-surfaces (a surface for a discrete iso-value) or 2D contour plots (a set of iso-contours).

### 2.3.3 Electronic reactivity descriptors

Looking into the electronic structure of the system, the reactivity descriptors can be described efficiently. In essence to this, the *d-band* model for the spin-polarized DFT calculations has been adopted to determine the electronic descriptors introduced by Bhattacharjee and co-workers (modification of Nørskov and Hammer *d-band* model) [29-30], i.e., *d-band center* ($\varepsilon_d$), *d-band width* ($W_d$) and *fractional filling* ($f_l$) *of d-band* (for both spin-up and spin-down states) for representative systems using Eqns. 2.27 and 2.29. The $\varepsilon_d$ was computed as the first moment of the density of states projected on the *d-band* about the Fermi level ($E_F$) and is expressed as,

$$\varepsilon_d = \frac{\int_{-\infty}^{E_F}(E - E_F)D_{d\sigma}(E)dE}{\int_{-\infty}^{E_F} D_{d\sigma}(E)dE} \tag{2.27}$$

The $W_d$ was computed as the square root of the second moment of the *d-band* density of states projected on the *d-band* about the $\varepsilon_d$ and is expressed as,

$$W_d = \frac{\int_{-\infty}^{E_F} D_{d\sigma}(E)[(E - E_F) - \varepsilon_d]^2 dE}{\int_{-\infty}^{E_F} D_{d\sigma}(E)dE} \tag{2.28}$$

The $f_l$ was taken as the integral overstates up to the Fermi level divided by the integral over all states as,

$$f_l = \frac{\int_{-\infty}^{E_F} D_{d\sigma}(E)dE}{\int_{-\infty}^{\infty} D_{d\sigma}(E)dE} \tag{2.29}$$

where, $D_{d\sigma}(E)$ ($\sigma = \uparrow,\downarrow$) is the DOS projected on the d-states of the TM, E is the energy and $E_F$ is the Fermi energy of the system. Figure 2.6 illustrates the schematic of the spin-polarized DOS of the transition metal with the electronic reactivity descriptors.

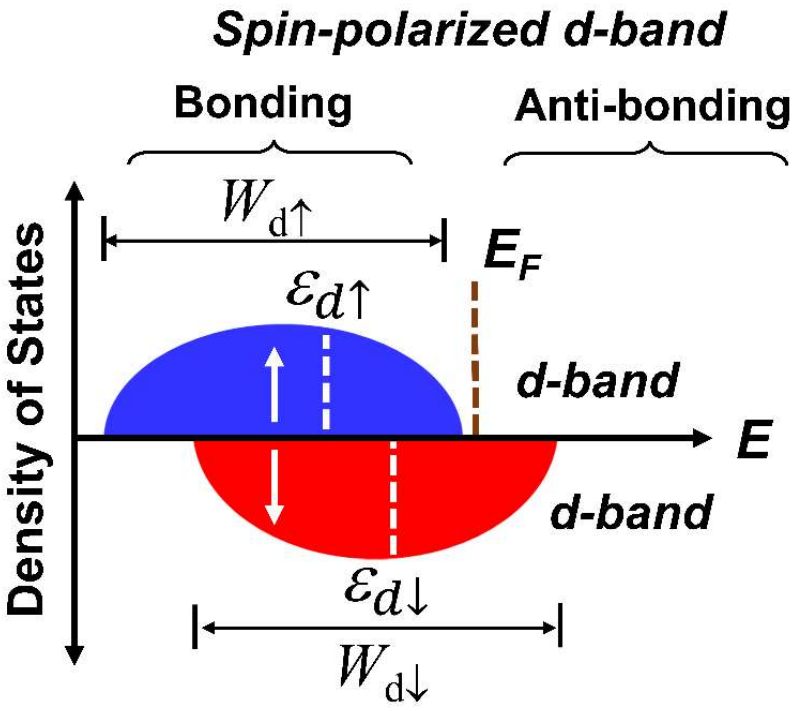


Figure 2.6: Schematic illustration of the spin-polarized DOS of the transition metal with the electronic reactivity descriptors.

## 2.4 Density functional perturbation theory

Recently, the response of the atoms to electric fields has become applicable for interpreting macroscopic parameters such as linear optical properties [31]–the static dielectric tensor, the piezoelectric tensor, the vibrational frequencies, and the matrix of the Born effective charges. Density-functional perturbation theory (DFPT) or linear response (LR) theory for vibrational spectra starts from the following expression [32-33]:

$$\frac{\partial^2 E(\vec{R})}{\partial \vec{R}_i \partial \vec{R}_j} = \frac{\partial \vec{F}_i}{\partial \vec{R}_j} = \int \frac{\partial n_{\vec{R}}(\vec{r})}{\partial \vec{R}_j} \frac{\partial V_{\vec{R}}(\vec{r})}{\partial \vec{R}_i} d\vec{r} + \int n_{\vec{R}}(\vec{r}) \frac{\partial^2 V_{\vec{R}}(\vec{r})}{\partial \vec{R}_i \partial \vec{R}_j} d\vec{r} + \frac{\partial^2 E_{ion}(\vec{R})}{\partial \vec{R}_i \partial \vec{R}_j} \quad (2.30)$$

which relates the second derivatives of the total energy $E(\vec{R})$ to the ground-state electron density $n_{\vec{R}}(\vec{r})$ and to the linear response of the charge density to a displacement of the ions, $\partial n(\vec{r})/\partial \vec{R}_i$.

The $V_{\vec{R}}(\vec{r})$ stands for the electron-ion interaction and $E_{ion}(\vec{R})$ is the direct ion-ion interaction. Within DFPT, the charge-density and wave-function linear response to a perturbation of a wave-vector $\vec{q}$ is given by a closed set of equations which can be solved in terms of lattice-periodic functions and is decoupled from a similar equation for other Fourier components of the same perturbation. Only sums over occupied orbitals are involved [31]. In a *dipole approximation*, the intensity of the infrared active modes may be calculated [34] in terms of the oscillator strengths [35] determined by the Born effective charges and the displacement vectors:

$$I(\omega) = \sum_{\alpha=1}^{3} \mid \sum_{l=1}^{M} \sum_{\beta=1}^{3} Z^*_{\alpha\beta}(l)\, e_\beta(l) \mid^2 \quad (2.31)$$

where $e_\beta(l)$ is the normalized vibrational eigenvector of the $\omega^{th}$ mode, $\alpha$ and $\beta$ indicate the Cartesian polarizations, $l$ labels the different atoms of the system, and $Z^*_{\alpha\beta}(l)$ is the Born effective charge tensor of the $l^{th}$ atom. The ionic effective charges $Z^*_{\alpha\beta}(l)$ are from the computational point of view essentially the second derivatives of the energy of the molecule with respect to an applied electric field and the amplitude of a vibrational distortion. As such, they are directly accessible to second-order density-functional

perturbation theory (DFPT) [36-37], which looks to be a very powerful and accurate method to compute the vibrational properties of extended systems [38]. The Born effective charge [39] (also called a transverse or dynamic charge) of a crystalline system, defined as the induced polarization due to a unit sublattice displacement, is a fundamental quantity connecting the electrostatic fields of the lattice to its phononic properties [40]. It contains important information not only about the electronic structure and the bonding properties of the system but also about the coupling of its longitudinal- and transverse-optical phonon modes to the external infrared radiation. The $Z^*_{\alpha\beta}(l)$ is to be understood as a coefficient of proportionality between a change of macroscopic polarization in direction $\alpha$ caused by an atomic displacement in direction $\beta$ under conditions of zero external field. Furthermore, the intensity of each normal mode as a result of Eqn. (2.31) is a scalar number and it is directly comparable with experimental absorption intensities.

## 2.5 Transition state determination

### 2.5.1 Regular NEB method

An elastic band with $N+1$ images can be denoted by [$R_0$, $R_1$, $R_2$, . . ., $R_N$], where the end points, $R_0$ and $R_N$, are fixed and given by the energy minima corresponding to the initial and final states. The $N-1$ intermediate images are adjusted by the optimization algorithm. In the NEB method [41-42], the total force acting on an image is the sum of the spring force along the local tangent and the true force perpendicular to the local tangent,

$$F_i = F_i^s\big|_{\parallel} - \nabla E(R_i)\big|_{\perp} \tag{2.32}$$

where the true force is given by

$$\nabla E(R_i)|_{\perp} = \nabla E(R_i) - \nabla E(R_i)\cdot \hat{\tau}_i \tag{2.33}$$

Here, E is the energy of the system, a function of all the atomic coordinates, and $\widehat{\tau_i}$ is the normalized local tangent at image $i$. The spring force is

$$F_i^s|_{\parallel} = k(|R_{i+1} - R_i| - |R_i - R_{i-1}|) \cdot \hat{\tau}_i \quad (2.34)$$

where k is the spring constant. An optimization algorithm is then used to move the images according to the force in Eqn. (2.32). The images converge on the MEP with equal spacing if the spring constant is the same for all the springs. Typically, none of the images lands at or even near the saddle point, and the saddle point energy needs to be estimated by interpolation.

### 2.5.2 Climbing image NEB method

The climbing image NEB (CI-NEB) method constitutes a small modification to the NEB method. Information about the shape of the MEP is retained, but a rigorous convergence to a saddle point is also obtained. This additional feature does not add any significant computational effort. After a few iterations with the regular NEB, the image with the highest energy $i_{max}$ is identified. The force on this one image is not given by Eqn. (2.32) but rather by,

$$F_{i_{max}} = -\nabla E(R_{i_{max}}) + 2\nabla E(R_{i_{max}})|_{\parallel} = -\nabla E(R_{i_{max}}) + 2\nabla E(R_{i_{max}}) \cdot \hat{\tau}_{i_{max}} \hat{\tau}_{i_{max}} \quad (2.35)$$

This is the full force due to the potential with the component along with the elastic band inverted.

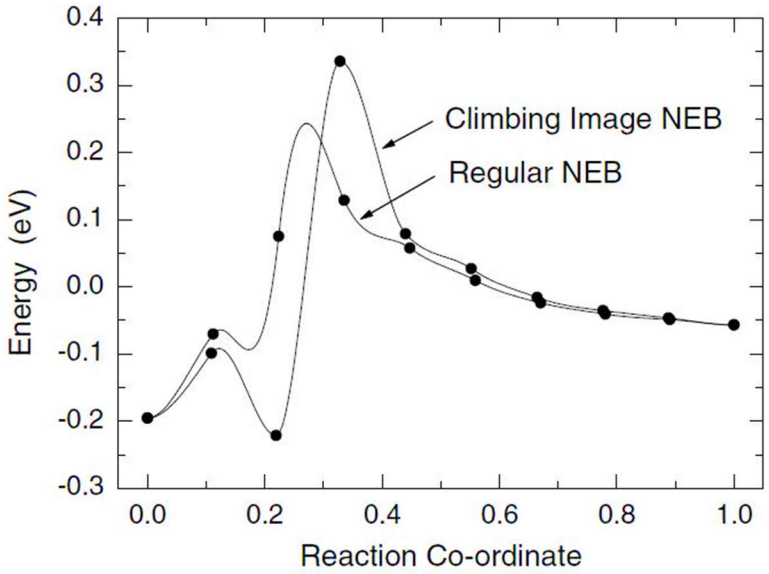


Figure 2.7: Density functional theory calculations of the minimum energy path for $CH_4$ dissociative adsorption on an Ir(111) surface [43].

The maximum energy image is not affected by the spring forces at all. Henkelman et al. [43] gave an example about the $CH_4$ molecule dissociated on the Ir(111) surface for comparing the calculated results from NEB and CI-NEB methods, as shown in Figure 2.7. It can be seen clearly from Figure 2.7 that the regular NEB results in a low resolution of the barrier, and the interpolation underestimate the activation energy. On the contrary, with the CI-NEB method, it is possible to locate the climbing image at the saddle point and to give a precise barrier. Obviously, CI-NEB method is better than the regular NEB method in searching transition state, which makes it a more appropriate choice for us to study the chemical reaction and to find the corresponding transition state. Qualitatively, the climbing image moves up the potential energy surface along the elastic band and down the potential surface perpendicular to the band. The other images in the band serve the purpose of defining the one degree of freedom for which maximization of the energy is carried out. Since the images in the band eventually converge to the MEP, they give a good approximation to the reaction coordinate around the saddle point. As long as the CI-NEB method converges, the climbing image will converge to the saddle point. Since all the images are being relaxed simultaneously, there is no additional cost of turning one of the images into a climbing image.

## 2.6 Computational codes and visualization softwares

This section contains the brief information and introduction of codes and visualization packages utilized throughout the thesis work.

- **Quantum ESPRESSO package**

The density functional theory calculations in this thesis are performed using the software package Quantum ESPRESSO [44-45], which is an Open-Source Package and is freely available to researchers around the world under the terms of the GNU General Public License.

All the structural (optimization), relative energetic, electronic, magnetic, adsorption properties, and especially catalytic activity presented in this thesis have been calculated using this package.

- **GAUSSIAN09 package**

**Gaussian** is a very popular and widely used simulation software due to its user-friendly interface to predict energies, molecular structures, spectroscopic data (NMR, IR, UV, etc), and much more advanced calculations. It is released in 1970 by John Pople and his research group at Carnegie-Mellon University as **Gaussian 70**. It has been continuously updated. In this thesis work, calculations of Raman spectra and optical properties of pure and bimetallic nanoclusters have been investigated using the **Gaussian09** package [46].

- **FDMNES package**

Finite Difference Method Near-Edge Structure (FDMNES) is a user-friendly *ab initio* (uses DFT) code [47-48] devoted to the simulation of the K edges of all the chemical elements. In this thesis work, XANES spectra of pure and bimetallic nanoclusters were calculated using the finite difference method (FDM) and Hedin−Lundqvist exchange−correlation potential as implemented in the FDMNES ab initio package.

Throughout the thesis, all the pictorial representations of structures, HOMO-LUMO, and charge density differences were prepared using the XCrySDen [49] and Vesta visualization packages [50].

## References


1. F. Giustino, Materials Modelling Using Density Functional Theory: Properties and Predictions, Oxford University Press, (2014).
2. J. C. Slater, Quantum Theory of Molecules and Solids: Electronic Structure of Molecules, McGraw-Hill, (1963).
3. E. Schrödinger, *Phys. Rev.* **28**, 1049-1070, (1926).
4. H. Sadeghi, *Nanotechnology* **29**, 373001-373032, (2018).
5. M. Born, J. R. Oppenheimer, *Ann. Physik.* **84**, 457-484, (1927).
6. P. Hohenberg, W. Kohn, *Phys. Rev.* **136**, 864-871, (1964).
7. W. Kohn, L. J. Sham, *Phys. Rev.* **140**, 1133-1138, (1965).
8. D. M. Ceperley, B. J. Alder, *Phys. Rev. Lett.* **45**, 566-569, 1980.
9. J. P. Perdew, A. Zunger, *Phys. Rev. B.* **23**, 5048-5079, (1981).
10. J. P. Perdew, K. Burke, M. Ernzerhof, *Phys. Rev. Lett.* **77**, 3865–3868, (1996).
11. J. P. Perdew, Y. Wang, *Phys. Rev. B* **45**, 13244–13249, (1992).
12. Y. Zhang, W. Yang, *Phys. Rev. Lett.* **80**, 890, (1998).
13. B. Hammer, L. B. Hansen, J. K. Nørskov, *Phys. Rev. B.* **59**, 7413 –7421, (1999).
14. J. C. Phillips, L. Kleinman, *Phys. Rev.* **116**, 287-294, (1959).
15. R. M. Martin, Electronic Structure: Basic Theory and Practical Methods, (Cambridge University Press, Cambridge, 2004).
16. G. Kresse, D. Joubert, *Phys. Rev. B.* **59**, 1758-1775, (1999).
17. P. E. Blöchl, *Phys. Rev. B.* **50**, 17953-17979, (1994).
18. R. P. Feynman, *Phys. Rev.* **56**, 340–343, (1939).
19. J. D.Head, M. C. Zerner, *Chem. Phys. Lett.* **122**, 264-270, (1985).
20. J. B. Foresman, Æ. Frisch, Exploring Chemistry with Electronic Structure Methods, 3rd ed., Gaussian, Inc.: Wallingford, CT, 2015.
21. M. M. Pant, A. K. Rajagopal. *Solid State Commun.* **10**, 1157–1160, (1972).
22. U. V. Barth, L. Hedin, *J. Phys. C: Solid State Phys.* **5**, 1629–1642, (1972).
23. S. Grimme, *J. Comput. Chem.* **27**, 1787-1799. (2006).
24. S. Grimme, J. Antony, S. Ehrlich, H. A. Krieg, *J. Chem. Phys.* **132**, 154104-154119, (2010).
25. O. Jepsen, O. K. Andersen, *Solid State Commun.* **9**, 1763-1767, (1971).
26. P. E. Blöchl, O. Jepsen, O. K. Andersen, *Phys. Rev. B* **49**, 16223-16233, (1994).
27. M. Methfessel, T. Paxton, *Phys. Rev. B* **40**, 3616-3621, (1989).
28. T. Edvinsson, *R. Soc. Open Sci.* **5**, 180387-180404, (2018).

29. B. Hammer, J. K. Nørskov, Theoretical Surface Science and Catalysis-Calculations and Concepts. *Adv. Catal.* **45**, 71-129, (2000).
30. S. Bhattacharjee, U. V. Waghmare, S. C. Lee, *Sci. Rep.* **6**, 35916-35925, (2016).
31. M. Gajdos, K. Hummer, G. Kresse, J. Furthmuller, F. Bechstedt, *Phys. Rev. B* **73**, 045112-045121, (2006).
32. S. Baroni, S. de Gironcoli, A. D. Corso, P. Giannozzi, *Rev. Mod. Phys.* **73** 515-562, (2001).
33. R. Pick, M. H. Cohen, R.M. Martin, *Phys. Rev. B* **1**, 910-920, (1970).
34. G. Kresse, J. Furthmuller, J. Hafner, *Europhys. Lett.* **32**, 729-734, (1995).
35. P. Bruesch, Phonons: Theory and Experiments II, Springer, (1986).
36. S. Baroni, P. Giannozzi, A. Testa, *Phys. Rev. Lett.* **58**, 1861-1864, (1987).
37. P. Giannozzi, S. de Gironcoli, P. Pavone, S. Baroni, *Phys. Rev. B* **43**, 7231-7242, (1990).
38. P. Giannozzi, S. Baroni, *J. Chem. Phys.* **100**, 8537-8539, (1994).
39. M. Born, K. Huang, Dynamical Theory of Crystal Lattices, Oxford University Press, (1954).
40. A. Shukla, *Phys. Rev. B* **61**, 13277-13282, (2000).
41. H. Jonsson, G. Mills, K.W. Jacobsen, in Classical and Quantum Dynamics in Condensed Phase Simulation, World Scientific (1998).
42. G. Henkelman, H. Jonsson, *J. Chem. Phys.* **113**, 9978-9985, (2000).
43. G. Henkelman, B. P. Uberuaga, H. Jonsson, *J. Chem. Phys.* **113**, 9901–9904, (2000).
44. P. Giannozzi, S. Baroni, N. Bonini, M. Calandra, R. Car, C. Cavazzoni, D. Ceresoli, G. L. Chiarotti, M. Cococcioni, I. Dabo, et al., *J. Phys.: Condens. Matter* **21**, 395502-395521, (2009).
45. P. Giannozzi, O. Andreussi, T. Brumme, O. Bunau, N. M. Buongiorno, M. Calandra, R. Car, C. Cavazzoni, D. Ceresoli, M. Cococcioni, et al. *J. Phys.: Condens. Matter* **29**, 465901-465930, (2017).
46. M. J. Frisch, G. W. Trucks, H. B. Schlegel, G. E. Scuseria, M. A. Robb, J. R. Cheeseman, G. Scalmani, V. Barone, B. Mennucci, G. A. Peterssonet, et al., Gaussian 09, Revision **D.01**, 1–20, (2013).
47. Y. Joly, *Phys. Rev. B* **63**, 125120-125130, (2001).
48. O. Bunaau, Y. Joly, *J. Phys.: Condens. Matter* **21**, 345501-345512, (2009).
49. A. Kokalj, *J. Mol. Graphics Modell.* **17**, 176-179, (1999).
50. K. Momma, F. Izumi, *J. Appl. Crystallogr.* **44**, 1272-1276, (2011).